Results in Physics 87 (2026) 108697

Contents lists available at ScienceDirect

Results in Physics

journal homepage: www.elsevier.com/locate/rinp

^{40}Ar+p Elastic scattering measurement at energies near the Coulomb barrier for optical potential study

D. Kim [a,b], S. Ahn [a,*], J.W. Lee [a], H.Y. Lee [a], G.M. Gu [a,c], Y.H. Song [d], S.W. Hong [c,d], D.S. Ahn [a,1], C. Akers [d], S.M. Cha [a], K.Y. Chae [c], Y. Cho [e], S. Choi [a], S. Do [f,a], K.I. Hahn [a,b], J.W. Hwang [a], Y. Jang [a,f], M.S. Kwag [d], C.H. Kim [c], D.G. Kim [d], E. Kim [d], J.C. Kim [d], M.J. Kim [a], M. Kim [d], S.H. Kim [c], Y. Kim [a], Y.H. Kim [a], C.S. Lee [d], J. Lee [a,f], K.B. Lee [d], S. Lee [d], C.Y. Lim [d], G.H. Oh [d], M. Park [a,g], S.J. Park [d], X. Pereira-Lopez [a], S.J. Pyeon [d], T. Shin [d], C.W. Son [d], K. Tshoo [d], J. Won [a]

[a] Center for Exotic Nuclear Studies, Institute for Basic Science, Daejeon, 34126, Republic of Korea
[b] Department of Science Education, Ewha Womans University, Seoul, 03760, Republic of Korea
[c] Department of Physics, Sungkyunkwan University, Suwon, 16419, Republic of Korea
[d] Institute for Rare Isotope Science, Institute for Basic Science, Daejeon, 34000, Republic of Korea
[e] Department of Physics and Astronomy, Seoul National University, Seoul, 08826, Republic of Korea
[f] Department of Physics, Korea University, Seoul, 02841, Republic of Korea
[g] Department of Physics, Ewha Womans University, Seoul, 03760, Republic of Korea

ARTICLE INFO

Keywords:
Elastic scattering
Nucleon–nucleus optical potentials
Global optical model potentials
RAON
KoBRA
ELARK
Cross-section measurements

ABSTRACT

Nuclear optical potentials are essential for calculating nuclear cross-sections and for probing nuclear structures and dynamics. The phenomenological global optical model potentials (pGOMPs), such as Koning–Delaroche (KD) and Perey–Perey (PP) potentials, have been extensively tested and are generally accepted. However, optical potentials extrapolated at low energies where data do not exist are not always reliable. This study aims to measure new ^{40}Ar+p elastic scattering data at low energies near the Coulomb barrier to extract optical model potential parameters. The elastic scattering of ^{40}Ar+p in inverse kinematics was performed at energies of 4.4, 5.9, and 8.3 MeV/u using KoBRA at the RAON facility. The ELARK barrel-type silicon detector array was employed to detect scattered protons. The angular distributions of the elastic scattering cross-sections were analyzed and compared with those calculated using the GOMPs. Our measured angular distributions could not be reproduced by pGOMPs at low energies. The experimental angular distributions were analyzed to extract optical potential parameters via χ^2 minimization, which were subsequently shown to satisfy the dispersion relation. The results show the limitations of the pGOMPs at lower energies near the Coulomb barrier and indicate the need for further studies of optical potentials with more experimental data to improve the reliability of pGOMPs in reproducing experimental observations.

Introduction

The nuclear optical model is a fundamental framework in nuclear physics, providing a key input for the calculation of angular distributions of elastic and inelastic cross-sections, as well as various reaction cross-sections. For example, it plays a crucial role in analyzing transfer reactions through the use of the distorted wave Born approximation, where absorption and refraction phenomena of wavefunctions in the entrance and exit channels can be properly addressed by the distorted waves calculated from the optical model. Therefore, establishing reliable optical potentials is essential for studying nuclear structure and reaction dynamics.

In principle, optical potentials can be deduced by analyzing individual elastic scattering data for various combinations of projectiles, targets, and incident energies. The optical model potentials obtained in this way have successfully described numerous elastic and inelastic scattering phenomena of stable nuclei using complex effective potentials. However, the challenges in measuring the elastic cross-sections

* Corresponding author.
E-mail address: ahnt@ibs.re.kr (S. Ahn).
[1] Present address: Facility for Rare Isotope Beams, Michigan State University, East Lansing, Michigan 48824, USA.

https://doi.org/10.1016/j.rinp.2026.108697
Received 15 December 2025; Received in revised form 25 April 2026; Accepted 28 May 2026
Available online 3 June 2026
2211-3797/© 2026 The Authors. Published by Elsevier B.V. This is an open access article under the CC BY-NC license (http://creativecommons.org/licenses/by-nc/4.0/).

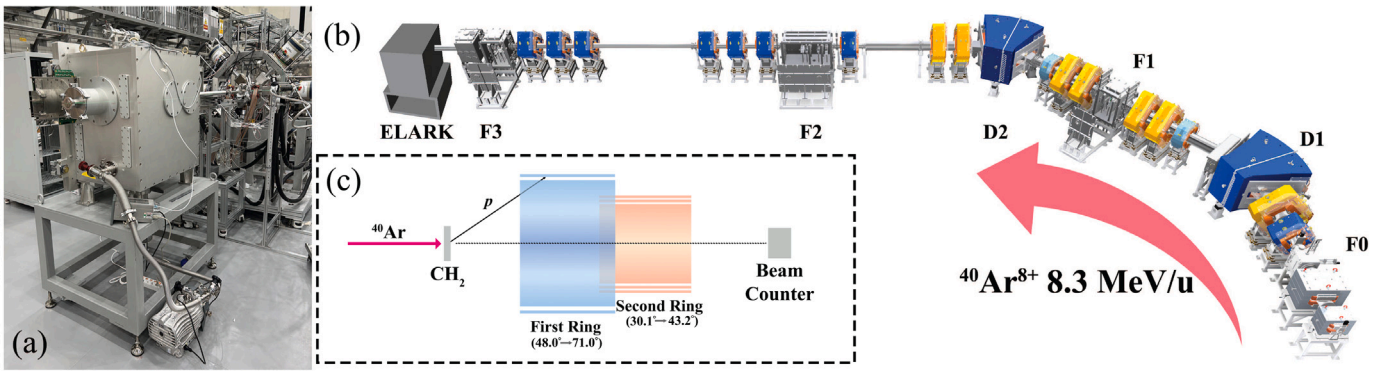


Fig. 1. (a) ELARK chamber located on the downstream side of the F3 chamber. (b) Schematic view of the KoBRA beamline. (c) Schematic view of the target position and detector arrangement.

for all possible combinations of nuclear systems and the limited experimental data far from the valley of stability have hindered the progress. To overcome these challenges, systematic analysis of extensive scattering data has been performed, revealing systematic trends in potential parameters as a function of the target nucleus's mass, charge, and the incident energy. Such efforts led to the development of so-called phenomenological global optical model potentials (pGOMPs) [1–4].

The pGOMP is parameterized as smooth functions of the target's mass number (A) and atomic number (Z), the projectile type (proton or neutron), and the incident beam energy (E). This approach provides a useful description of the scattering data across a wide range of variables. Several models have been introduced to describe proton elastic scattering, including the Becchetti–Greenlees model [1], the spherical CH89 model [2], Perey–Perey (PP) model [3], and the Koning–Delaroche (KD) model [4]. The KD model is one of the most widely used optical potentials and was developed to provide a universal potential based on extensive experimental data, effectively describing nuclei with $24 < A < 209$ and projectile energies up to approximately 200 MeV.

Although pGOMPs have generally been effective, they exhibit certain limitations. Since these potentials are calibrated exclusively with experimental data from stable isotopes, extrapolating the parameters to unstable isotopes introduces significant uncertainties. The incomplete coverage of experimental data in certain energy ranges and for specific projectile–target systems limits the reliability of the pGOMP parameters, highlighting the need for further validation. For example, while many experiments have been reported for the elastic scattering of ^{40}Ar+p [5–10], there are no experimental data in the low-energy range of 4 to 7 MeV. Given that the Coulomb barrier for the ^{40}Ar + p system is approximately 4 MeV in the center-of-mass frame, it is important to note that non-elastic channels begin to open just above this threshold. As a result, the optical model parameters in the near-barrier regime may deviate significantly from those extracted at higher incident energies, where absorption into non-elastic channels is more pronounced and gradual. The lack of elastic scattering measurements in this low-energy region means that proton pGOMPs, primarily constrained by data at higher energies, are not benchmarked near the Coulomb barrier. Consequently, their reliability in this regime is uncertain, and obtaining precise elastic scattering data at energies just above the barrier is essential. Such measurements can provide critical constraints for verifying or refining pGOMP parametrizations and, ultimately, enhancing their reliability near the Coulomb barrier.

Another approach introduced by Koning and Delaroche is the use of local optical model potentials (LOMPs), constructed by adjusting the global parameterization for each specific isotope, based on the availability of sufficient elastic scattering data [4]. These local fits demonstrated improved agreement with experimental angular distributions by exploiting the analytically defined energy dependence of the potential. Nevertheless, the use of LOMPs is still limited in cases where experimental data are rare or absent. For systems such as ^{40}Ar+p, where elastic scattering data are lacking near the Coulomb barrier, it is not possible to derive a reliable LOMP at low energies. In such cases, the authors of the LOMPs recommended employing the global OMP with reasonable confidence [4].

The motivation of the present study is to measure the angular distributions of elastically scattered protons from ^{40}Ar + p at previously unexplored low incident energies (4.4, 5.9, and 8.3 MeV/u) near the Coulomb barrier. The experimental results are compared to the predictions from the KD and PP global optical model to assess the validity of these models at these low energies and to extract optimum optical potential parameters. Also, we note that this report is the first physics result of experiments utilizing beams accelerated at the Rare isotope Accelerator complex for ON-line experiments (RAON) facility [11–15].

Experimental setup

The ^{40}Ar + p elastic scattering experiment was conducted at the Korea Broad acceptance Recoil spectrometer and Apparatus (KoBRA) beamline [16–18] at RAON. KoBRA is one of the experimental facilities at RAON and supports precision measurements of nuclear reactions by using advanced spectrometers and detector systems. After the beam commissioning of the Super-Conducting Linac (SCL3) [19], RAON has recently marked a significant achievement by successfully delivering both stable and rare isotope beams.

The ^{40}Ar ions were produced from an Electron Cyclotron Resonance ion source and accelerated by the SCL3, reaching a beam energy of 8.3 MeV/u. The beam intensity from the SCL3 was 10^9 pps but was moderated to 10^7 pps at the F0 focal plane of KoBRA using a 10^2 attenuator, to prevent damage to the target located downstream of the F3 focal plane of KoBRA (see Fig. 1 for focal planes). Parallel Plate Avalanche Counters (PPACs) at each focal plane were used to monitor the beam during the tuning. Possible target degradation was assessed by monitoring the elastic-scattering yield over time, and no significant change within statistical uncertainty (5%) was observed. The beam energy was measured by the two dipole magnets, D1 and D2 shown in Fig. 1. Aluminum degraders with thicknesses of 46.3 μm and 30.2 μm were positioned at the F0 focal plane to reduce the beam energy to 4.4 and 5.9 MeV/u, respectively. The systematic uncertainty of the beam energy was 2.4%, obtained as the quadratic sum of the uncertainty in the dipole-magnet $B\rho$ value and the energy-distribution width measured at the F1 PPAC. Energy straggling in the Al degraders is included in the energy distribution measured by the PPAC.

For this experiment, polyethylene (CH_2) targets with thickness of 0.199 and 0.152 mg/cm^2 and a diameter of 20 mm were used. The thickness was determined by measuring the energy loss of α particles emitted from a ^{241}Am α source. The effective beam size was constrained by the size of the target, leading to systematic uncertainties of 5% in the solid angle coverage of the silicon detectors and angular uncertainties

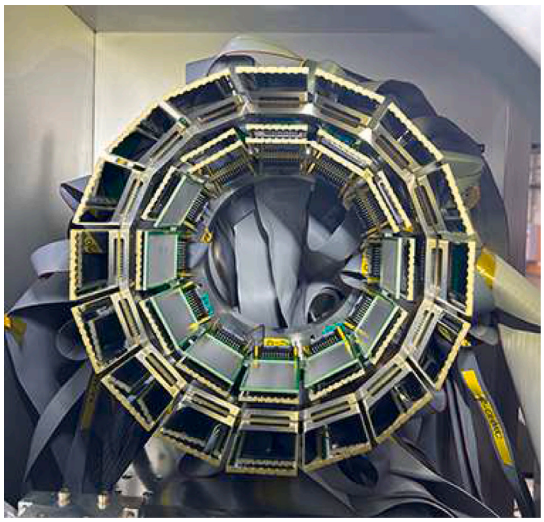


Fig. 2. Experimental setup for the elastic scattering experiments using the ELARK system. The majority of the scattered protons were detected at angles near 90 degrees.

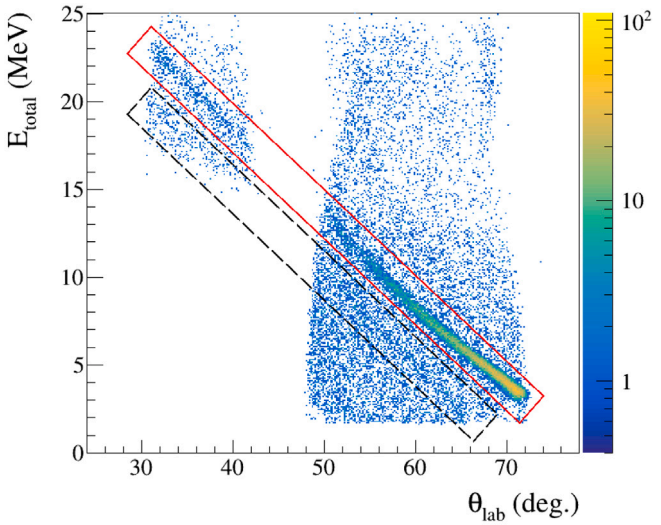


Fig. 3. Spectrum of charged particle energy (E_{total}) deposited in silicon detectors as a function of laboratory angles (θ_{lab}) for E_{lab} = 8.3 MeV/u. The spectrum above 45 degrees was obtained from one of the detectors in the first ring, while the spectrum below 45 degrees was obtained from one of the ΔE-E telescopes in the second ring. The spectrum enclosed by the red solid line and black dashed line correspond to protons scattered elastically and inelastically, respectively.

of 2.5 degrees in particle angle. In the analysis, uncertainties from the target thickness were also taken into account.

Elastically scattered protons were detected by using a barrel-type silicon detector array, ELastic scattering detector ARray in inverse Kinematics (ELARK), as shown in Fig. 2, designed to provide high angular resolution and wide angle coverage. The ELARK array has two rings: the first ring consists of 16 single silicon detectors, and the second ring is composed of 12 ΔE-E telescopes. The 16 silicon detectors are X6 detectors [20], developed by Micron Semiconductor Ltd, covering angles from 48 to 71 degrees in the laboratory frame. Eight out of the 12 ΔE-E telescopes are equipped with CENS Single-sided silicon Detectors (CSDs) of 500 or 700-μm thickness, along with X6 detectors of 1000-μm thickness, to detect low-energy protons from the scattering in case of beam energies at E_{lab} = 4.4 and 5.9 MeV/u. The remaining four telescopes consist of two X6 (1000-μm) detectors to count the high-energy protons scattered at the beam energy of E_{lab} = 8.3 MeV/u. These 12 ΔE-E telescopes cover angles from 30.1 to 43.2 degrees.

The X6 detector employed eight resistive strips on the junction side for position measurement along the beam axis and four non-resistive strips on the ohmic side for energy measurement in this experiment. The position resolution was better than 1 mm, and the energy resolution was around 150 keV Full Width at Half Maximum (FWHM) at E = 5.48 MeV of α-particles emitted from a ^{241}Am α source. The CSD detectors were only used to identify scattered particles with the ΔE-E technique, thus low-energy protons stopped in the CSDs were excluded from the angular distribution analysis.

Experimental results

Elastically scattered protons were measured at forward laboratory angles (θ_{lab} < 90 degrees). The energy of the scattered protons was observed as a function of angles for each beam energy covering center-of-mass (CM) angular range from 40 to 120 degrees except angles between 80 and 100 degrees due to a geometric limitation of the detector configuration. Fig. 3 clearly shows proton bands from elastic and inelastic scattering events.

Fig. 4 shows a reconstructed Q-value distribution for the ^{40}Ar + p scattering. A peak was observed at Q = 0 MeV, corresponding to the elastic scattering channel. The first excited state of ^{40}Ar also appeared at Q = −1.4 MeV for the inelastic scattering channel. In this paper, we only considered the elastic scattering channel.

Angular distributions can be extracted by the number of proton events for a given solid angle, the number of beam particles, and the target areal density. The differential cross-section at each angle bin is given by

$$\left(\frac{\Delta\sigma}{\Delta\Omega}\right)_i = \frac{N_i^p}{\Delta\Omega_i\, N_{\text{beam}}\, n_{\text{target}}} = \frac{N_i^p}{\Delta\Omega_i\, N_s}, \tag{1}$$

where N_i^p, $\Delta\Omega_i$, N_{beam}, n_{target}, and N_s denote the proton yield in the ith angular bin, the corresponding solid angle, the number of beam particles, the target areal density, and the normalization coefficient ($N_s \equiv N_{\text{beam}}\, n_{\text{target}}$), respectively. The proton yield was obtained by fitting the elastic data in the ith angular bin. The angle bin size in the CM frame was set to 4–6 degrees to balance the resolution and statistical reliability considering the uncertainty of 2.5 degrees, derived from the maximum beam size at the target. The relative systematic uncertainty was propagated through the same expression in quadrature as

$$\left(\frac{\Delta(\Delta\sigma/\Delta\Omega)}{\Delta\sigma/\Delta\Omega}\right)^2_{\text{sys}} = \left(\frac{\Delta t}{t}\right)^2 + \left(\frac{\Delta\Omega}{\Omega}\right)^2 + \left(\frac{\Delta N_{\text{fit},i}}{N_i^p}\right)^2, \tag{2}$$

where each term on the right-hand side corresponds to target-thickness (Δt), solid-angle ($\Delta\Omega$), and signal-fitting ($\Delta N_{\text{fit},i}$) contributions, respectively. The angular uncertainty of 2.5 degrees was determined from the maximum effective beam spot on target, constrained by the 20 mm target diameter, and this angular spread was propagated through the solid-angle term.

Owing to the high instantaneous beam rate of 10^9 pps associated with a 1% beam duty factor, direct measurement of the beam intensity during the experiment was not feasible. Consequently, the beam normalization coefficient N_s in Eq. (1) could not be determined directly. Instead, the normalization coefficient N_s was estimated by analyzing the characteristics of elastic scattering, incorporating angular distribution data from previous experiments [8] as a reference. The analysis was constrained by the following criteria, the details of which are described below:

- The normalization coefficient N_s should fall within the range determined by fitting reasonable optical potential parameters to the scaled experimental angular distribution data.

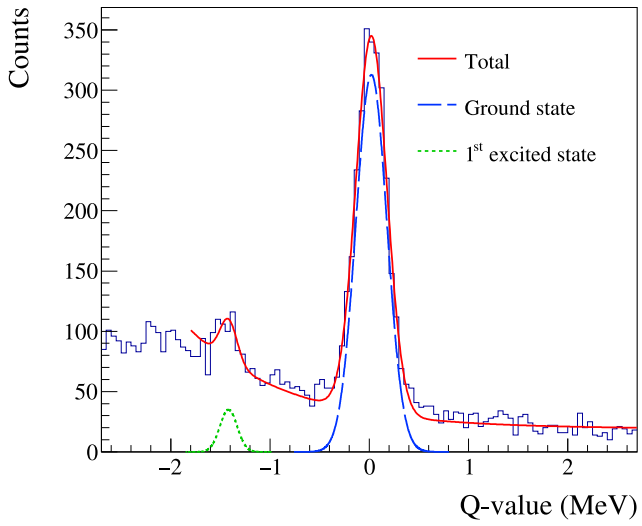


Fig. 4. The Q-value spectrum for the beam energy of 8.3 MeV/u at θ_{CM} = 57 – 92 degrees. The Q-value spectrum was employed to identify scattering events corresponding to the ground and excited states of ^{40}Ar. Together with the overall fitting (red solid line) of Q-value spectrum is shown the ground state (blue dashed line) at zero and the first excited state (green dotted line) corresponding to excitation energy of $Q = -1.42$ MeV.

- The total reaction cross-section, as obtained from the optical potential, is expected to exhibit a consistent and smooth energy dependence.
- The optical potential obtained from the experimental data should conform to the dispersion relation to ensure physical validity.

The optical model parameters were extracted in the angular range of 40 to 120 degrees by employing the minimum chi-square method to optimize the agreement between the calculated and experimental cross-sections, using the MINUIT [21] search algorithm as described in Ref. [22]. The χ^2 is defined by

$$\chi^2 = \sum_i \frac{(\sigma^i_{\text{exp}}(E,\theta) - \sigma^i_{\text{theory}}(E,\theta))^2}{(\Delta\sigma^i_{\text{exp}}(E,\theta))^2}, \tag{3}$$

where i runs through all possible angles for each energy.

In the fitting procedure, the imaginary volume term, W_v, was set to zero. At near-barrier energies, the elastic-scattering observables are primarily sensitive to surface absorption, while sensitivity to volume absorption is limited. In fact, the data required the resulting value of W_v parameter to be close to zero. We fixed $W_v = 0$ to avoid over-parameterization and unstable parameter correlations, and described absorption with the surface imaginary term. The geometrical shape parameters and spin–orbit strength were used from the KD pGOMP. With these parameters constrained across all energies, the depth parameters of the real volume terms and imaginary surface terms were varied to obtain optimal fitting results.

For the ^{40}Ar+p system, experimental differential cross-sections exist at E_{lab} = 7.77, 9.36, 10.5, and 14.1 MeV [8]. Thus, we first performed the optical model analyses for these existing experimental differential cross-section data and extracted the optical potential parameters, from which we could evaluate the reaction cross-sections at these energies. It is known that the reaction cross-sections in this energy range can be expressed by a smooth function of energy as described in Refs. [23–25]. Thus, by extracting the optical potentials from our experimental data, reaction cross-sections were calculated at E_{lab} = 4.4, 5.9, and 8.3 MeV, and compared with the evaluated reaction cross-sections at E_{lab} = 7.77, 9.36, 10.5, and 14.1 MeV. This comparison and requirement of reaction cross-sections being a smooth function of energy could fix the unknown normalization of our measured data. In other words, in the optical-model analyses, we treated the overall normalization factor as an additional unknown parameter, allowing the optical model calculations to reproduce not only the differential cross sections but also the total elastic-scattering cross sections. The normalization factor, N_s, was determined simultaneously with the optical potential parameters in a multidimensional parameter search using the minimum χ^2 method.

In this procedure, the modified Wong-formula fit is used as an auxiliary global smoothness (or consistency) constraint on $\sigma_R(E)$ to discriminate among candidate solutions, while the χ^2 fit to the angular distributions remains the primary observable for determining the optical parameters and the normalization. Thus, the modified Wong-formula constraint does not independently fix the normalization and introduces only limited model dependence. Within this constrained fitting framework, no alternative normalization choice was found that allows the KD or PP global parametrizations to reproduce the low-energy (4.4 and 5.9 MeV) data while satisfying the same constraints.

The extracted parameters at seven beam energies (including the four previously reported data sets) are summarized in Table 1, and the fitting results are plotted by the black solid lines in Fig. 5. For the previously reported data, the cross-section uncertainties were assigned as 5% of the data, following the guidelines provided in Ref. [8]. Although the average uncertainty in our cross-section data is approximately 8%–10%, this level of precision is typical for inverse kinematics measurements, as demonstrated by many prior studies which successfully extracted meaningful reaction and structure information from data with similar uncertainties [26–30].

Fig. 6 shows the reaction cross-sections evaluated by the optical model analyses which are denoted by black dots. The expression used in Refs. [23–25] reproduces the reaction cross-sections above the Coulomb barrier, but cannot be applicable near the Coulomb barrier. (Note that σ_R in Eq. (3) of Ref. [25] becomes zero at the Coulomb barrier and negative below the barrier.) Therefore, instead of using the expression given in the references, we adopted a modified Wong's formula [32] as follows and fitted the evaluated reaction cross-sections.

$$\sigma_R(E_{lab}) = \frac{(a + bE_{CM})^2}{2E_{CM}} \times \ln[1 + e^{c(E_{CM} - V_{cb})}], \tag{4}$$

where E_{lab}, V_{cb} and E_{CM} are the beam energy in the lab frame, Coulomb barrier, and CM energy, respectively. The values of the parameters a, b, and c are 2.79, −0.037, and 53.09, respectively, determined by fitting the evaluated reaction cross-sections. In Eq. (4), the Coulomb-barrier parameter V_{cb} was treated as a parameter and optimized to V_{cb} = 4.10 MeV. With this fitted V_{cb}, the energies studied in this work still span the near-barrier and above-barrier region in the CM frame ($E_{CM} \approx$ 4.29, 5.76, and 8.10 MeV). As a result, the reaction cross-sections $\sigma_R(E)$ obtained from this analysis demonstrate a smooth energy dependence as shown in Fig. 6.

While the beam normalization factor was fixed by comparing our data with the existing data, the optical model analysis showed that a reasonable consistency could be achieved. The σ_R calculated by the KD global optical potential at 4.4 MeV is significantly larger than σ_R evaluated by the extracted optical potential, which suggests a modification on the global optical potential parameters seems necessary.

Discussion

The experimental angular distributions of the elastically scattered protons by ^{40}Ar are illustrated in Fig. 5(a). The shape of the cross-sections evolves from high to low energies, with the nuclear elastic scattering cross-section decreasing. Consequently, for E_{lab} = 4.4 MeV, the diffraction pattern is not visible at $\theta_{CM} < 120$ degrees from our data.

In Fig. 5(b)–(d), the ratios of the differential cross-sections to the Rutherford cross-sections are plotted. Both PP (cyan dotted curve) and

Table 1
Extracted optical model parameters. Definitions of parameters are explained in Ref. [31]. The values of real volume (V) and imaginary surface (W_d) terms were varied during the fitting.

Energy (MeV)	V (MeV)	r_v (fm)	a_v (fm)	W_d (MeV)	r_d (fm)	a_d (fm)	V_{so} (MeV)	r_{so} (fm)	a_{so} (fm)	χ^2/N
4.4	58.1	1.19	0.672	0.050	1.29	0.540	5.75	0.996	0.590	3.66
5.9	43.2	1.39	0.430	5.97	1.87	0.368	5.75	0.996	0.590	0.85
7.77 [8]	55.8	1.19	0.672	6.35	1.29	0.540	5.75	0.996	0.590	16.45
8.3	57.5	1.19	0.672	8.02	1.29	0.540	5.75	0.996	0.590	4.07
9.36 [8]	55.1	1.19	0.672	8.21	1.29	0.540	5.75	0.996	0.590	10.48
10.5 [8]	56.0	1.19	0.672	8.63	1.29	0.540	5.75	0.996	0.590	5.94
14.1 [8]	52.0	1.19	0.672	8.96	1.29	0.540	5.75	0.996	0.590	3.62

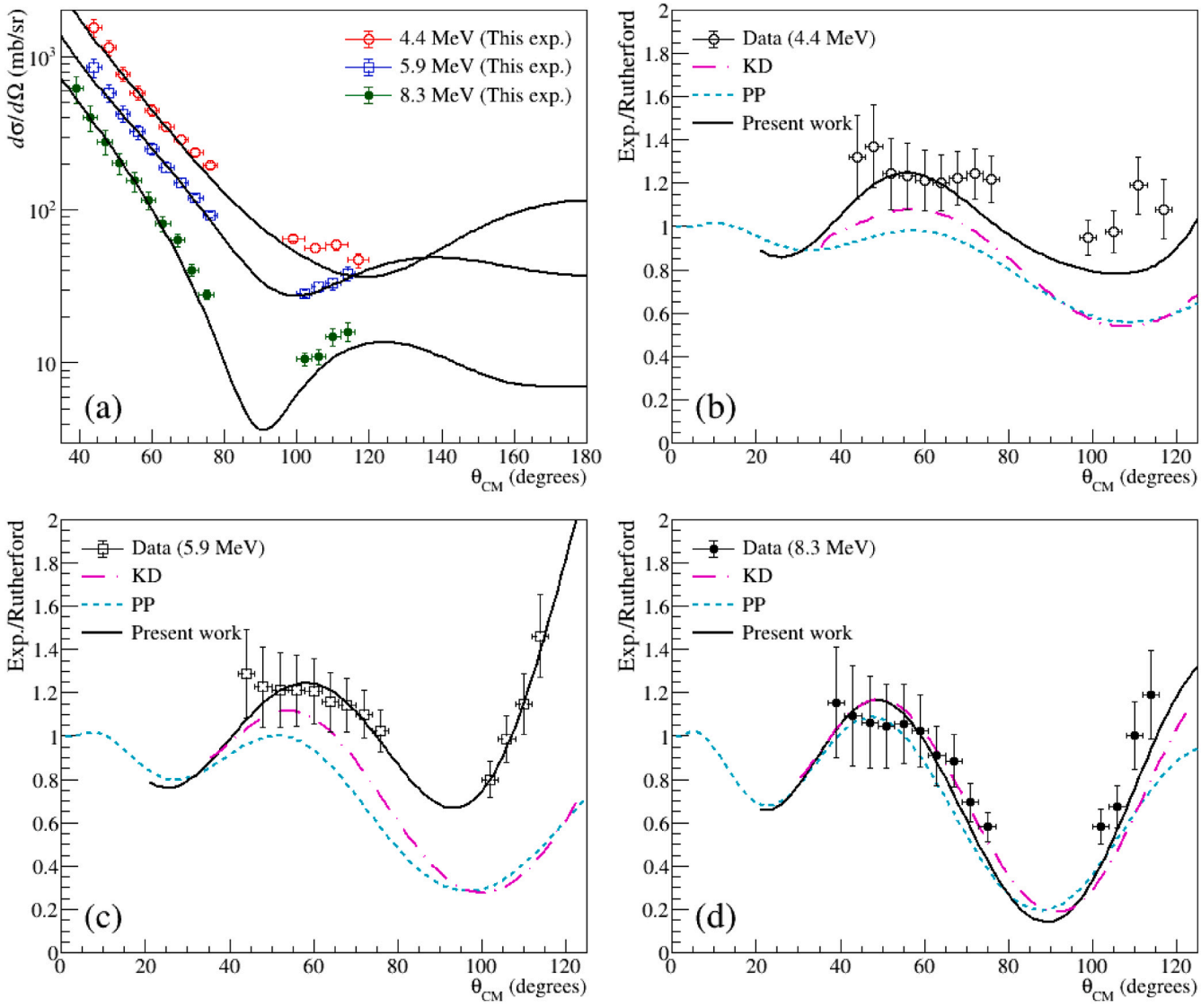


Fig. 5. The experimental differential cross-sections at 4.4, 5.9 and 8.3 MeV are plotted in (a), by the open circles, open squares, and filled circles, respectively, with error bars representing the combined statistical and systematic uncertainties. The black solid curves in (a) are the differential cross-sections using the optical potential parameters in Table 1. The ratios of the cross-sections to the Rutherford cross-sections are shown in (b)–(d) from this work (black solid curve), PP pGOMP (cyan dotted curve), and KD pGOMP(magenta dash-dotted curve). It can be seen that both PP and KD potentials can reproduce the experimental data quite well for 8.3 MeV, whereas they underestimate the data significantly for 4.4 and 5.9 MeV. Our optical potentials reproduce the cross-section for all three energy cases.

KD pGOMP(magenta dash-dotted curve) reproduce the experimental data at E_{lab} = 8.3 MeV for angles lower than 80 degrees, but not for large angles. At lower energies of 4.4 and 5.9 MeV both PP and KD potentials do not reproduce the experimental data. The KD LOMP parameters could not be employed for direct comparison, as no parameter set for ^{40}Ar is available in Ref. [4]. To explore the potential applicability of nearby isotopic systematics, the parameters for the ^{40}Ca+p system were used to calculate the elastic scattering cross section. However, the resulting predictions still exhibit large discrepancies, particularly at E_{lab} = 4.4 MeV and θ_{CM} < 100 degrees. These results show the limitations of both pGOMPs and LOMPs in achieving a satisfactory level of description at energies where data are not available.

It is well known that the real and imaginary parts of the optical potentials are related to each other through the dispersion relation,

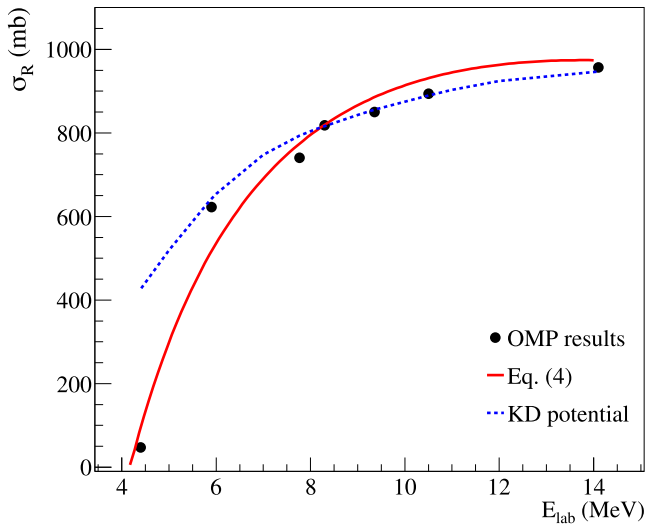


Fig. 6. The reaction cross-sections evaluated at E_{lab} = 4.4, 5.9, 8.3 MeV using the optical potentials extracted as described in the text are plotted with those evaluated at E_{lab} = 7.77, 9.36, 10.5, 14.1 MeV [8]. The optical potential parameters are given in Table 1. The KD potential reproduces the reaction cross-sections well except at E_{lab} = 4.4 MeV. The modified Wong's formula in Eq. (4) reproduces the reaction cross-sections at all energies. The points labeled "OMP results" denote values evaluated from the OMP, not directly measured total cross-sections.

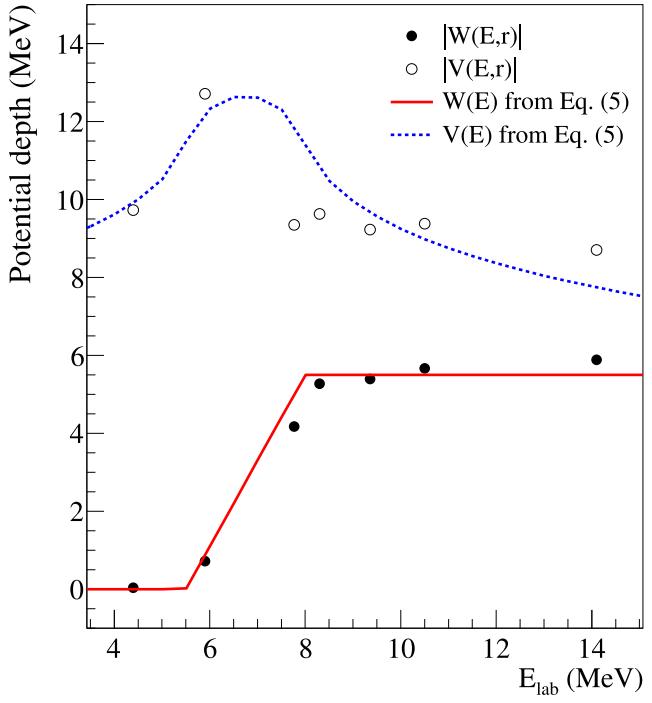


Fig. 7. The dispersion relation between the real (V) and imaginary (W) parts of the optical potential evaluated at r = 5.13 fm, as determined in the present work. The calculated potentials (red solid and blue dashed lines) from Eq. (5) are shown to reproduce the extracted values (open and filled circles).

which comes from the causality [33–35]. The variations of the values of the real and imaginary potentials near the Coulomb barrier are well explained by the dispersion relation. The open (filled) circles in Fig. 7 denote the values of the real (imaginary) potentials evaluated at r = 5.13 fm by using the parameters in Table 1 for various energies. The values of the imaginary potentials plotted by the filled circles can be approximately represented by the red line shown in Fig. 7. The real part of the potential can be calculated by the dispersion relation:

$$V(E) = V(E_s) + \frac{E - E_s}{\pi} \mathcal{P} \int_0^\infty dE' \, \frac{W(E')}{(E' - E_s)(E' - E)}, \quad (5)$$

where $\mathcal{P}$ stands for the principal value and $V(E_s)$ is the value of the real potential at a reference energy $E = E_s$. The $V(E_s)$ was set to 11.46 MeV when E_s = 5.5 MeV. The resulting real potential is plotted by the blue dashed line, which reproduces the values of the real potentials (open circles) extracted by the optical model analyses. The dispersion relation analyses were performed in other radii as well, and similar results as shown in Fig. 7 were obtained. Thus, our optical potential parameters are shown to satisfy the dispersion relation. Mahaux and Sartor showed that the threshold anomaly was observed not only for heavy projectiles but also for proton projectiles, such as in the case of ^{40}Ca + p [36]. We also observed this phenomenon in our experimental data for ^{40}Ar + p scattering.

The newly determined optical potential parameters exhibit significant improvement in reproducing the experimental data in comparison with the PP and KD pGOMP models. Our results show the necessity of improvement in the pGOMP to predict both differential and reaction cross-sections. To draw definitive conclusions, further experimental investigations at low energies near the Coulomb barrier are needed.

Summary

The ^{40}Ar+p elastic scattering experiment utilizing the KoBRA beamline at the RAON facility was performed to measure differential cross-sections near the Coulomb barrier and to extract new optical potential parameters. The ELARK barrel-type silicon detector array enabled measurements of the angular distributions and energy spectra of the elastic scattering. The experimental cross-sections measured at low energies (E_{lab} = 4.4, 5.9, and 8.3 MeV/u) were obtained for the first time and employed in the optical model analysis.

The results show that the nuclear elastic scattering cross-section diminishes with decreasing incident beam energy, as evidenced by the disappearance of the diffraction pattern at low energies (e.g., at E_{lab} = 4.4 MeV/u, where no diffraction is observed below 120 degrees in the CM frame). When the experimental differential cross-section ratios relative to Rutherford scattering were compared with the predictions from the PP and KD pGOMPs, both models adequately reproduced the data at forward angles for E_{lab} = 8.3 MeV/u but failed at larger angles and at lower energies of 4.4 and 5.9 MeV/u, indicating the limitations of pGOMP models in these regimes. The beam normalization factor was indirectly determined by analyzing the elastic scattering angular distributions and fitting the data with the optical model, together with a modified Wong's formula to calculate the total reaction cross-sections.

The newly extracted optical potential parameters were further validated by demonstrating that the real and imaginary parts satisfy the dispersion relation. Overall, our phenomenological optical potentials show significantly better agreement with the experimental data than the PP and KD pGOMPs, emphasizing the need for further investigations at low energies near the Coulomb barrier to refine these models for reliable cross-section calculations.

CRediT authorship contribution statement

D. Kim: Writing – review & editing, Writing – original draft, Validation, Project administration, Investigation, Data curation, Conceptualization. **S. Ahn:** Writing – review & editing, Writing – original draft, Supervision, Project administration, Formal analysis, Data curation, Conceptualization. **J.W. Lee:** Writing – review & editing, Software, Formal analysis, Data curation. **H.Y. Lee:** Resources, Investigation. **G.M. Gu:** Investigation, Data curation. **Y.H. Song:** Writing – review

& editing, Writing – original draft, Validation, Methodology. **S.W. Hong:** Writing – review & editing, Writing – original draft, Validation, Methodology, Formal analysis. **D.S. Ahn:** Writing – review & editing, Investigation. **C. Akers:** Investigation. **S.M. Cha:** Investigation, Data curation. **K.Y. Chae:** Investigation, Data curation. **Y. Cho:** Investigation, Data curation. **S. Choi:** Investigation, Data curation. **S. Do:** Investigation, Data curation. **K.I. Hahn:** Writing – review & editing, Investigation, Funding acquisition, Data curation. **J.W. Hwang:** Software, Data curation. **Y. Jang:** Investigation, Data curation. **M.S. Kwag:** Investigation. **C.H. Kim:** Investigation, Data curation. **D.G. Kim:** Investigation. **E. Kim:** Investigation. **J.C. Kim:** Investigation. **M.J. Kim:** Investigation. **M. Kim:** Investigation, Data curation. **S.H. Kim:** Investigation, Data curation. **Y. Kim:** Methodology. **Y.H. Kim:** Investigation, Data curation. **C.S. Lee:** Investigation. **J. Lee:** Investigation, Data curation. **K.B. Lee:** Investigation. **S. Lee:** Investigation. **C.Y. Lim:** Investigation. **G.H. Oh:** Investigation. **M. Park:** Methodology. **S.J. Park:** Investigation. **X. Pereira-Lopez:** Writing – review & editing, Software, Investigation, Data curation. **S.J. Pyeon:** Investigation. **T. Shin:** Investigation. **C.W. Son:** Investigation. **K. Tshoo:** Investigation. **J. Won:** Investigation, Data curation.

Declaration of competing interest

The authors declare that they have no known competing financial interests or personal relationships that could have appeared to influence the work reported in this paper.

Acknowledgments

This work was supported in part by the Institute for Basic Science (IBS) (Project Codes IBS-I001-01 and IBS-R031-D1) and the National Research Foundation of Korea (Grant Nos. 2013M7A1A1075764, NRF-2016R1A2B3008343, RS-2024-00338255, and RS-2024-00436392), funded by the Ministry of Science and ICT (MSIT) of the Republic of Korea. This research used resources from the RAON facility, a user facility operated by the Institute for Rare Isotope Science of IBS. The authors thank the RAON facility operations staff for their dedicated support, which was instrumental in making the measurements possible.

Data availability

Data will be made available on request.

References

[1] Becchetti FD, Greenlees GW. Nucleon-nucleus optical-model parameters, $a > 40$, $e < 50$ MeV. Phys Rev 1969;182:1190–209. http://dx.doi.org/10.1103/PhysRev.182.1190, URL https://link.aps.org/doi/10.1103/PhysRev.182.1190.

[2] Varner R, Thompson W, McAbee T, Ludwig E, Clegg T. A global nucleon optical model potential. Phys Rep 1991;201(2):57–119. http://dx.doi.org/10.1016/0370-1573(91)90039-O, URL https://www.sciencedirect.com/science/article/pii/037015739190039O.

[3] Perey C, Perey F. Compilation of phenomenological optical-model parameters 1954–1975. At Data Nucl Data Tables 1976;17(1):1–101. http://dx.doi.org/10.1016/0092-640X(76)90007-3, URL https://www.sciencedirect.com/science/article/pii/0092640X76900073.

[4] Koning A, Delaroche J. Local and global nucleon optical models from 1 kev to 200 MeV. Nucl Phys A 2003;713(3):231–310. http://dx.doi.org/10.1016/S0375-9474(02)01321-0, URL https://www.sciencedirect.com/science/article/pii/S0375947402013210.

[5] Keyworth G, Kyker G, Bilpuch E, Newson H. A high-resolution study of isobaric analogue resonances in 41k. Nucl Phys 1966;89(3):590–608. http://dx.doi.org/10.1016/0029-5582(66)90934-5, URL https://www.sciencedirect.com/science/article/pii/0029558266909345.

[6] Okumuşoğlu N, Birchall J, Al-Ghazi M, Lapointe C, Mckee J, Conzett H, Larimer R, Von Rossen P. The elastic scattering of polarised protons by 40ar. Nucl Phys A 1983;393(1):45–51. http://dx.doi.org/10.1016/0375-9474(83)90063-5, URL https://www.sciencedirect.com/science/article/pii/0375947483900635.

[7] Rush A, Burge E, Smith D. Elastic and inelastic scattering of 30 and 50 mev polarized and unpolarized beams of protons by 40ar and 14n. Nucl Phys A 1971;166(2):378–92. http://dx.doi.org/10.1016/0375-9474(71)90438-6, URL https://www.sciencedirect.com/science/article/pii/0375947471904386.

[8] Oda Y, Takeda M, Takano N, Yamazaki T, Hu C, Kikuchi K, Kobayashi S, Matsuda K, Nagahara Y. Elastic and inelastic scattering of protons from n, ne, mg, si, s and a in the energy range from 7.6 MeV to 14.2 MeV. J Phys Soc Japan 1960;15(5):760–71. http://dx.doi.org/10.1143/JPSJ.15.760.

[9] Barnard A, Kim C. Elastic scattering and reactions of protons on argon-40. Nucl Phys 1961;28(1):428–37. http://dx.doi.org/10.1016/0029-5582(61)91063-X, URL https://www.sciencedirect.com/science/article/pii/002955826191063X.

[10] Freier GD, Famularo KF, Zipoy DM, Leigh J. Elastic scattering of protons by a^{40}. Phys Rev 1958;110:446–7. http://dx.doi.org/10.1103/PhysRev.110.446, URL https://link.aps.org/doi/10.1103/PhysRev.110.446.

[11] Kwon YK, Choi BH, Choi CJ, Chung YS, Han JE, Hong IS, Hwang WJ, Jeon D, Joo J, Jung HC, Kang BH, Kim BC, Kim DG, Kim GD, Kim HJ, Kim MJ, Kim SK, Kim YK, Kim YJ, Lee JH, Park SJ, Park YH, Seo CS, Woo HJ, Yun CC. Status of rare isotope science project in Korea. Few-Body Syst 2013;54(7):961–6. http://dx.doi.org/10.1007/s00601-013-0605-5.

[12] Jeon D, Hong IS, Kim HJ, Kim JW, Bodenstein RM, Cha HJ, Choi SJ, Choi S, Choi OR, Do H, Choi BH, Choi CJ, Han J, Han WK, Hyun MO, Jang H, Joo JD, Joung MJ, Jung HC, Jung YC, Kim DG, Kim E, Kim H, Kim JH, Kim JY, Kim WK, Kim Y, Kim M, Kim MJ, Lee JH, Lee KW, Lee MK, Park GT, Ryu S, Shin I, Shin JH, Song J-S, Yoon S, Yi K-H, Yun CC, Zaghloul A, Kim SK, Matlabjon S, Park GS, Bahng JB, Hwang JG, Jang SW, Kim ES. Design of the RAON accelerator systems. J Korean Phys Soc 2014;65(7):1010–9. http://dx.doi.org/10.3938/jkps.65.1010.

[13] Jeong S, Papakonstantinou P, Ishiyama H, Kim Y. A brief overview of RAON physics. J Korean Phys Soc 2018;73(4):516–23. http://dx.doi.org/10.3938/jkps.73.516.

[14] Kwon M, Chung YS, Kwon YK, Shin TS, Sohn YU. RAON, Korean heavy ion accelerator facility. J Part Accel Soc Jpn 2021;17(4):293–301. http://dx.doi.org/10.50868/pasj.17.4_293.

[15] Chung Y, Kim H, Kwon M. Current status of the RAON low-energy heavy ion accelerator. J Korean Phys Soc 2022;80(8):693–7. http://dx.doi.org/10.1007/s40042-021-00373-y.

[16] Tshoo K, Chae H, Park J, Moon JY, Kwon YK, Souliotis GA, Hashimoto T, Akers C, Berg GPA, Choi S, Jeong SC, Kato S, Kim YK, Kubono S, Lee KB, Moon C-B. Design status of KOBRA for rare isotope production and direct measurements of radiative capture cross sections. Nucl Instrum Methods Phys Res B 2016;376:188–93. http://dx.doi.org/10.1016/j.nimb.2015.12.025, URL https://www.sciencedirect.com/science/article/pii/S0168583X15012707.

[17] Tshoo K, Pyeun SJ, Lee KB, Akers C, Park J, Kwag MS, Kim M, Kim JC, Kim DG, Kim YK, Ham C, Shin T, Lee S, Ahn S, Hwang JW, Ahn DS, Kim DH, Hahn KI, Kwon M. Recent progress in the construction of KoBRA for low-energy nuclear physics experiments. Nucl Instrum Methods Phys Res B 2023;541:56–60. http://dx.doi.org/10.1016/j.nimb.2023.05.005, URL https://www.sciencedirect.com/science/article/pii/S0168583X23002045.

[18] Hwang JW, Ahn S, Ahn DS, Kim D, Hahn KI, Tshoo K, Kwag M. KoBRA Wien filter for low-energy RI beam production and recoil separation. Nucl Instrum Methods Phys Res B 2023;541:1–3. http://dx.doi.org/10.1016/j.nimb.2023.04.042, URL https://www.sciencedirect.com/science/article/pii/S0168583X23001829.

[19] Chung YS, Kang J, Kwon M, Kwon E, Kwon JW, Kim GD, Kim DG, Kim MS, Kim S, Kim Y, Kim YH, Kim Y, Kim JW, Kim J, Kim H, Kim HJ, Kim H, Do H, Park MJ, Park BS, Park I, Park H, Bae SY, Baek BY, Seo CS, Seol KT, Son KT, Son C, Son HJ, Shin JH, Ahn Y, Yang KS, Woo HJ, Yoo JH, Yoon J, Lee DY, Lee MK, Lee SG, Lee YH, Lee JW, Lee J, Lim EH, Jang JH, Jang HM, Jang H, Jeon D, Jeon S, Jung Y, Jung HC, Jo KH, Jo HC, Jo YW, Cho JH, Joo JD, Jin H, Choi S, Choi O, Choi YJ, Choi JW, Choi CJ, Han J, Heo JI, Hyun MO, Hong IS, Ki T, Kim DM, Moon S, Yoon S, Lee S, Choi HS. Status of the RAON heavy-ion accelerator. J Korean Phys Soc 2024. http://dx.doi.org/10.1007/s40042-024-01207-3.

[20] Pereira-Lopez X, Ahn S, Ahn DS, Bae S, Cha SM, Hahn KI, Hwang JW, Kim D, Kim MJ, Lee HY, Moon B, Park C. Development and characterization of new position-sensitive silicon strip detectors. Nucl Instrum Methods Phys Res Sect B 2023;541:134–6. http://dx.doi.org/10.1016/j.nimb.2023.05.009, URL https://www.sciencedirect.com/science/article/pii/S0168583X23002069.

[21] James F, Roos M. Minuit - a system for function minimization and analysis of the parameter errors and correlations. Comput Phys Comm 1975;10(6):343–67. http://dx.doi.org/10.1016/0010-4655(75)90039-9, URL https://www.sciencedirect.com/science/article/pii/0010465575900399.

[22] Thompson IJ. Coupled reaction channels calculations in nuclear physics. Comput Phys Rep 1988;7(4):167–212. http://dx.doi.org/10.1016/0167-7977(88)90005-6, URL https://www.sciencedirect.com/science/article/pii/0167797788900056.

[23] Kox S, Gamp A, Cherkaoui R, Cole A, Longequeue N, Menet J, Perrin C, Viano J. Direct measurements of heavy-ion total reaction cross sections at 30 and 83 MeV/nucleon. Nucl Phys A 1984;420(1):162–72. http://dx.doi.org/10.1016/0375-9474(84)90663-8, URL https://www.sciencedirect.com/science/article/pii/0375947484906638.

[24] Mittig W, Chouvel JM, Long ZW, Bianchi L, Cunsolo A, Fernandez B, Foti A, Gastebois J, Gillibert A, Gregoire C, Schutz Y, Stephan C. Measurement of total reaction cross sections of exotic neutron-rich nuclei. Phys Rev Lett 1987;59:1889–91. http://dx.doi.org/10.1103/PhysRevLett.59.1889, URL https://link.aps.org/doi/10.1103/PhysRevLett.59.1889.

[25] Villari A, Mittig W, Plagnol E, Schutz Y, Lewitowicz M, Bianchi L, Fernandez B, Gastebois J, Gillibert A, Stephan C, Tassan-Got L, Audi G, Zhan W, Cunsolo A, Foti A, Belezyorov A, Lukyanov S, Penionzhkevich Y. Measurements of reaction cross sections for neutron-rich exotic nuclei by a new direct method. Phys Lett B 1991;268(3):345–50. http://dx.doi.org/10.1016/0370-2693(91)91588-M, URL https://www.sciencedirect.com/science/article/pii/037026939191588M.

[26] Thomas JS, Arbanas G, Bardayan DW, Blackmon JC, Cizewski JA, Dean DJ, Fitzgerald RP, Greife U, Gross CJ, Johnson MS, Jones KL, Kozub RL, Liang JF, Livesay RJ, Ma Z, Moazen BH, Nesaraja CD, Shapira D, Smith MS, Visser DW. Single-neutron excitations in neutron-rich ^{83}Ge and ^{85}Se. Phys Rev C 2007;76:044302. http://dx.doi.org/10.1103/PhysRevC.76.044302, URL https://link.aps.org/doi/10.1103/PhysRevC.76.044302.

[27] Jones KL, Adekola AS, Bardayan DW, Blackmon JC, Chae KY, Chipps KA, Cizewski JA, Erikson L, Harlin C, Hatarik R, Kapler R, Kozub RL, Liang JF, Livesay R, Ma Z, Moazen BH, Nesaraja CD, Nunes FM, Pain SD, Patterson NP, Shapira D, Shriner JF, Smith MS, Swan TP, Thomas JS. The magic nature of 132Sn explored through the single-particle states of 133Sn. Nature 2010;465(7297):454–7. http://dx.doi.org/10.1038/nature09048.

[28] Kozub RL, Arbanas G, Adekola AS, Bardayan DW, Blackmon JC, Chae KY, Chipps KA, Cizewski JA, Erikson L, Hatarik R, Hix WR, Jones KL, Krolas W, Liang JF, Ma Z, Matei C, Moazen BH, Nesaraja CD, Pain SD, Shapira D, Shriner JF, Smith MS, Swan TP. Neutron single particle structure in ^{131}Sn and direct neutron capture cross sections. Phys Rev Lett 2012;109:172501. http://dx.doi.org/10.1103/PhysRevLett.109.172501, URL https://link.aps.org/doi/10.1103/PhysRevLett.109.172501.

[29] Ahn S, Bardayan DW, Jones KL, Adekola AS, Arbanas G, Blackmon JC, Chae KY, Chipps KA, Cizewski JA, Hardy S, Howard ME, Kozub RL, Manning B, Matoš M, Nesaraja CD, O'Malley PD, Pain SD, Peters WA, Pittman ST, Rasco BC, Smith MS, Spassova I. Direct neutron capture cross section on ^{80}Ge and probing shape coexistence in neutron-rich nuclei. Phys Rev C 2019;100:044613. http://dx.doi.org/10.1103/PhysRevC.100.044613, URL https://link.aps.org/doi/10.1103/PhysRevC.100.044613.

[30] Manning B, Arbanas G, Cizewski JA, Kozub RL, Ahn S, Allmond JM, Bardayan DW, Chae KY, Chipps KA, Howard ME, Jones KL, Liang JF, Matos M, Nesaraja CD, Nunes FM, O'Malley PD, Pain SD, Peters WA, Pittman ST, Ratkiewicz A, Schmitt KT, Shapira D, Smith MS, Titus L. Informing direct neutron capture on tin isotopes near the $N = 82$ shell closure. Phys Rev C 2019;99:041302. http://dx.doi.org/10.1103/PhysRevC.99.041302, URL https://link.aps.org/doi/10.1103/PhysRevC.99.041302.

[31] Woods RD, Saxon DS. Diffuse surface optical model for nucleon-nuclei scattering. Phys Rev 1954;95:577–8. http://dx.doi.org/10.1103/PhysRev.95.577, URL https://link.aps.org/doi/10.1103/PhysRev.95.577.

[32] Wong CY. Interaction barrier in charged-particle nuclear reactions. Phys Rev Lett 1973;31:766–9. http://dx.doi.org/10.1103/PhysRevLett.31.766, URL https://link.aps.org/doi/10.1103/PhysRevLett.31.766.

[33] Mahaux C, Ngô H, Satchler G. Causality and the threshold anomaly of the nucleus-nucleus potential. Nucl Phys A 1986;449(2):354–94. http://dx.doi.org/10.1016/0375-9474(86)90009-6, URL https://www.sciencedirect.com/science/article/pii/0375947486900096.

[34] Mahaux C, Ngô H, Satchler G. Radial and energy dependence of the dispersive contributions to the α + 16o and α + 40Ca potentials near the threshold anomaly. Nucl Phys A 1986;456(1):134–58. http://dx.doi.org/10.1016/0375-9474(86)90370-2, URL https://www.sciencedirect.com/science/article/pii/0375947486903702.

[35] Kim BT, So WY, Hong SW, Udagawa T. Semiclassical character and optical model description of heavy ion scattering, direct reactions, and fusion at near-barrier energies. Phys Rev C 2002;65:044607. http://dx.doi.org/10.1103/PhysRevC.65.044607, URL https://link.aps.org/doi/10.1103/PhysRevC.65.044607.

[36] Mahaux C, Sartor R. Dispersion relation approach to the extrapolation towards negative energy of the optical potential in 40Ca and 208pb. Nucl Phys A 1986;460(3):466–500. http://dx.doi.org/10.1016/0375-9474(86)90425-2, URL https://www.sciencedirect.com/science/article/pii/0375947486904252.